minerals

MDPI

Article

Saprotrophic Fungus Induces Microscale Mineral Weathering to Source Potassium in a Carbon-Limited Environment

Jocelyn A. Richardson [1], Christopher R. Anderton [2] and Arunima Bhattacharjee [2,*]

[1] Stanford Synchrotron Radiation Lightsource, SLAC National Accelerator Laboratory, Menlo Park, CA 94025, USA; jocelynr@slac.stanford.edu
[2] Environmental Molecular Sciences Division, Earth and Biological Sciences Directorate, Pacific Northwest National Laboratory, Richland, WA 99354, USA; christopher.anderton@pnnl.gov
* Correspondence: arunimab@pnnl.gov

Abstract: Plants rely on potassium for many critical biological processes, but most soils are potassium limited. Moving potassium from the inaccessible, mineral-bound pool to a more bioavailable form is crucial for sustainably increasing local potassium concentrations for plant growth and health. Here, we use a synthetic soil habitat (mineral doped micromodels) to study and directly visualize how the saprotrophic fungus, *Fusarium sp. DS 682*, weathers K-rich soil minerals. After 30 days of fungal growth, both montmorillonite and illite (secondary clays) had formed as surface coatings on primary K-feldspar, biotite, and kaolinite grains. The distribution of montmorillonite differed depending on the proximity to a carbon source, where montmorillonite was found to be associated with K-feldspar closer to the carbon (C) source, which the fungus was inoculated on, but associated with biotite at greater distances from the C source. The distribution of secondary clays is likely due to a change in the type of fungal exuded organic acids; from citric to tartaric acid dominated production with increasing distance from the C source. Thus, the main control on the ability of *Fusarium sp. DS 682* to weather K-feldspar is proximity to a C source to produce citric acid via the TCA cycle.

Keywords: mineral-microbe interactions; simulated soil; *Fusarium*; bio-induced mineral transformation; synthetic soil habitat; XANES spectroscopy; synchrotron-XRF imaging

Citation: Richardson, J.A.; Anderton, C.R.; Bhattacharjee, A. Saprotrophic Fungus Induces Microscale Mineral Weathering to Source Potassium in a Carbon-Limited Environment. *Minerals* **2023**, *13*, x. https://doi.org/10.3390/xxxxx

Academic Editor(s):

Received: date
Revised: date
Accepted: date
Published: date

1. Introduction

Nitrogen, phosphorus, and potassium are essential elements for plant growth that can only be obtained through plant roots within soil. However, these elements are scarce and have limited bioavailability in the soil environment. As a result, a majority of agriculturally important crops are grown through the aid of fertilizers. Consequently, global nitrogen–phosphorus–potassium (NPK) fertilizers are at record prices and, in particular, the United States uses more K fertilizer than N or P compared to other global consumers [1]. Although K fertilizers are mined from mineral sources and are not viewed as a limited resource, political-economic status and supply-chain issues put pressure on access and cost. In addition, K mining and fertilizer production contributes to food-related greenhouse gas emissions [2]. Thus, there is considerable interest to find alternative, sustainable practices to increase local nutrient supply that is naturally present in soils.

Potassium is persistently limited in most environments since a majority of K (96–98%) is non-bioavailable, where it is structurally bound in soil minerals [3,4]. Second, the loss of K through harvesting or deforestation is greater than K input to soil [5–7]. Considering the natural abundance of K minerals in soil, converting non-bioavailable mineral-bound K (e.g., in K-feldspar and micas) to readily available (e.g., K in interlayer secondary clays, K in neoformed minerals or sorbed K) and to plant bioavailable K (K^+ in porewater) sources is a logical pathway to increase K accessibility to plants. However, abiotic mineral

weathering is too slow with respect to crop growing seasons [8,9], and although there are a number of studies into the presence of soil K-solubilizing microbes (KSM), resulting in greater K abundance in plants [7,10–17], there is a lack of understanding of the time and spatial scales over which KSM can actively increase bioavailable K [18–20]. Estimates of K solubilization in vitro have shown an increase in K solubilization from mineral surfaces by KSM within 5 days of incubation [17], surface physical and chemical alteration of 10s of μm sized muscovite grains in 15 days [21], and partial dissolution of K-rich micas and clay surfaces within 21 days [14]. Over longer timescales (1 year), field studies have indicated that fungal hyphae activity resulted in nm-μm layers of secondary mineral formation, although abiotic processes could not be ruled out [22]. Nevertheless, a number of these previous studies lack: (1) evidence of bio-induced secondary mineral formation; (2) the specific pathway from non-bioavailable to plant available K because of limitations in analytical methods; (3) appropriate rhizosphere-process spatial and temporal scales (i.e., sub-micron scale processes, or long temporal scales). As such, improving the resolution of the spatial characterization of the microbial processes governing K mineral dissolution and subsequent K bioavailability is essential for our understanding of the rhizosphere K cycle.

Previously, we developed mineral-doped microfluidic based synthetic soil habitats (SSHs), where we demonstrated fungal bridging of carbon (C) hotspots in a C- and water-limited environment [23]. The heterogeneity and opacity of soils create a central challenge in spatially analyzing the biotic and abiotic elements of soils, which is essential to investigate mechanisms driving biogeochemical processes. The SSHs reproduce key features of soil microenvironments, reducing the complexity of the soil matrix to facilitate spatial probing of biogeochemical processes, such as biotic mineral weathering. In addition, SSHs are amenable to various external environmental conditions (such as replicating drought), to study the effect of climate change on soil processes. Here, we used a SSH embedded with K-rich soil minerals (a natural kaolinite, composed of K-feldspar, and micas) and the saprotrophic fungi *Fusarium sp. DS 682* to visualize μm to mm scale biotic K transformations over 30 days in C-limited conditions. In line with recent studies using SSHs [23,24], we place our results within a rhizosphere framework to better understand microbial processes on nutrient cycling.

2. Materials and Methods

2.1. Micromodel Fabrication and Sample Preparation

The SSH was fabricated as described previously [23], using soft lithography techniques, and is composed primarily of polydimethylsiloxane (PDMS). Natural kaolinite (Sigma Aldrich, St. Louis, USA), composed of kaolinite, K-feldspar, biotite, and quartz [23] was embedded in the SSH to provide multiple K-rich mineral sources and to represent the chemical heterogeneity of the soil environment more accurately. Deep reactive ion etching (DRIE) of the SSH exposed mineral grains at the surface of the device to be accessible to fungal hyphae. *Fusarium sp. DS 682* [25] was inoculated at a nutrient port containing potato dextrose agar (PDA) at one end of the microfluidic channel (Figure 1A). A secondary PDA nutrient port was located at the opposite end of the SSH channel, approximately 3 cm from the inoculation port (not shown in Figure 1A, see [23] for further details). The channel was not saturated with media and fungal hyphae grew in the space between the inoculation and secondary nutrient ports. Previously we observed that fungi can only bridge between the inoculation and secondary nutrient port when natural kaolinite is embedded in the SSH. In SSHs with no minerals present, fungi could not bridge to the secondary nutrient port [23]. Fungi were grown for 30 days in the SSH and lyophilized prior to analyses. Fungal biomass and associated exudates were removed from the SSH surface by rinsing with chloroform for 5 min and subsequently with DI water (after optical imaging but before synchrotron analyses).

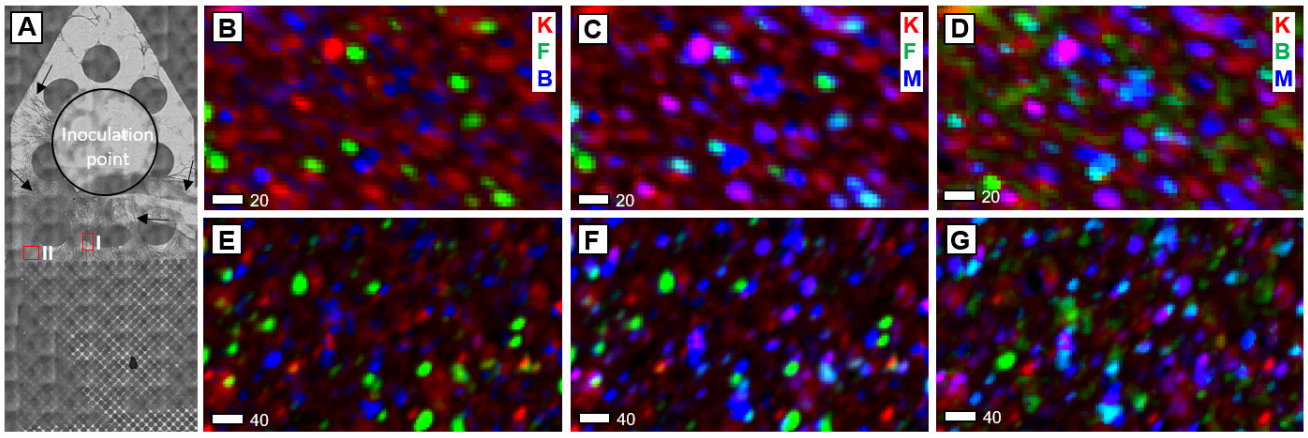

Figure 1. Potassium XRF images of SSH surface exposed to hyphae for 30 days. (**A**) Optical microscopy image of micromodel after 30 days, prior to the removal of hyphae. The edge of the inoculation point is denoted by the black circle. Arrows point to fungal hyphae which range in density across the SSH surface. Red boxes outline the regions mapped by XRF. Regions were chosen based on distance from inoculation point (carbon source) and hyphal density. (**B**–**D**) region I, (**E**–**G**) = region II. Column 1: kaolinite (K—red), feldspar (F—green) and biotite (B—blue). Column 2: kaolinite (K—red), feldspar (F—green) and montmorillonite (M—blue). Column 3: kaolinite (K—red), biotite (B—green) and montmorillonite (M—blue). In all maps, feldspar and kaolinite are scaled to the same total counts, which is 2× that of biotite and montmorillonite, which are scaled to the same counts as each other. Region I is rotated 90 degrees to the left compared to optical microscopy image. Scale bar is in microns.

2.2. Optical Microscopy Imaging of Fungal Hyphae

Fungal growth in the micromodels was imaged using a Nikon eclipse TE2000-E epifluorescence microscope (Nikon, Melville, NY, USA). Mosaic bright-field images were obtained using a 4× air objective and stitched across the length and width of the microchannel to capture fungal growth in micromodels (Figure 1A).

2.3. XRF Imaging and XANES Spectroscopy

To visualize mineral transformations on the SSH, we combined synchrotron multi-energy (ME) μ-X-ray Fluorescence (XRF) imaging (Figure 1B–G) with μ-X-ray Absorption Near Edge Structure (XANES) spectroscopy (Figure 2A,B) at the K, K-edge at the Stanford Synchrotron Radiation Lightsource (SSRL) beamline 14-3. A water-cooled double Si (111) crystal monochromator was used to select for the K, K-edge energy and calibrated using the white line of a natural kaolinite powder (3618.73 eV). Measurements were performed in a He-purged sample chamber (O_2 < 0.05%), with samples placed upright on a 360° rotating wheel, equipped with a Vortex 4-element Si drift detector. Energies for mapping were chosen based on features within the XANES spectra of natural kaolinite, K-feldspar and micas [26]. ME images were collected at 3615.7, 3617.25, 3618.4, 3620.15 and 3627.0 eV at a 5 μm spatial resolution at locations where hyphal biomass had differed in density, as well as from outside the channel where no hyphae grew as a control. Spots for XANES spectroscopy were chosen based on principal component analysis of the ME images to locate the spots of the most different K chemistries.

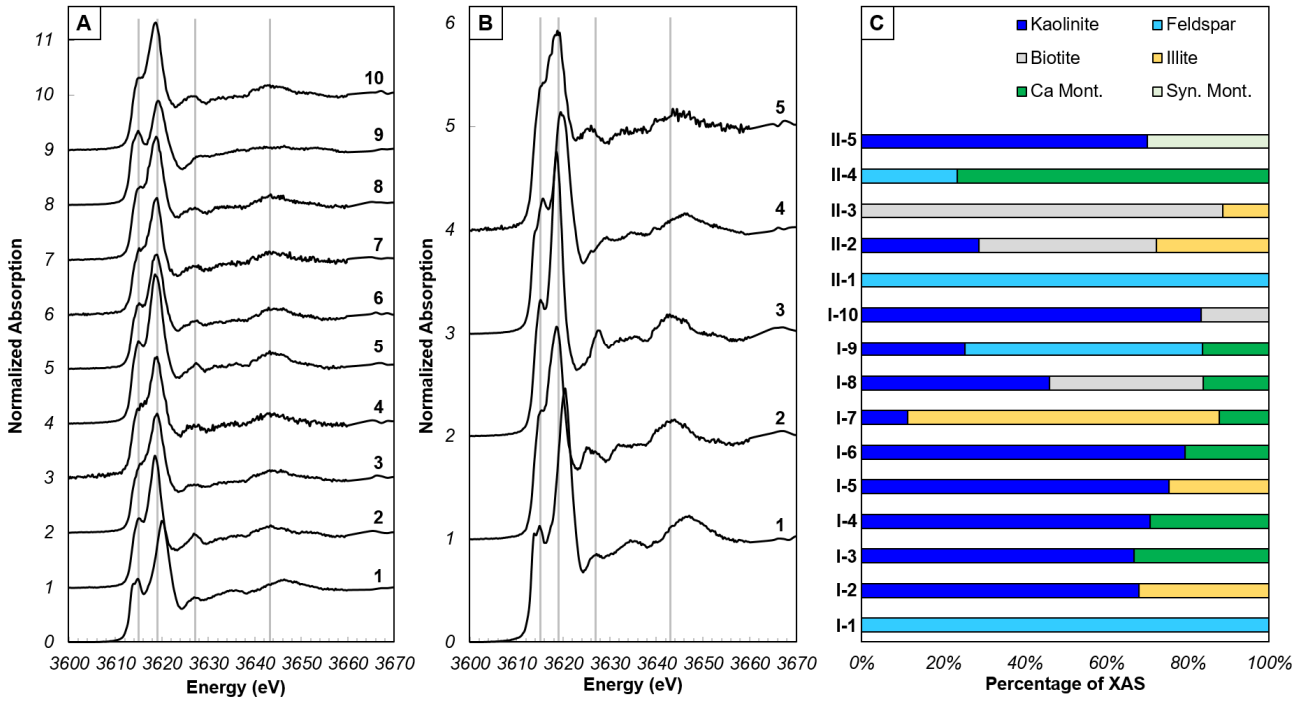

Figure 2. Potassium XANES spectra from spot locations within XRF map regions on SSH surface. (**A**) XANES spectra from region I. Grey lines represent energies of features in natural kaolinite powder (Figure S1). (**B**) XANES spectra from region II. Grey lines as in A. (**C**) Proportions of minerals that comprise each individual XANES spectrum, determined by LCF.

Data were processed in SixPACK [27] and Larch [28] (XANES), and SMAK [29] (XRF images) using standard methods [23]. Linear combination fitting (LCF) was performed in Larch using kaolinite powder and the following standard XANES spectra; biotite, muscovite, orthoclase, Ca- and Na-montmorillonite, synthetic mica montmorillonite, illlite-smectite wards vermiculite and llano vermiculite [30] (Figure S1). Reference spectra were obtained on samples from the Clay Minerals Society and Wards; see [30] for details on the source of each mineral used as a reference spectrum herein. Spectra from [30] were aligned to our dataset by aligning the first derivatives of kaolinite from their dataset to our calibration kaolinite and then applying the energy shift to all other standard spectra (E shift of 3.42 eV). The best fit results (Table S1) were determined by the R factor, number of standards used (where a smaller number of standards to satisfy the experimental XAS is preferred, when the R factor is not improved according to a Hamilton test), and visual inspection of fit. Although both Na- and Ca-montmorillonite, and biotite and muscovite were supplied during LCF, Ca-montmorillonite and biotite were exclusively used in the best fits when present. Similarly, despite including two vermiculite standards, neither was favored in the fits. Although vermiculite (Wards) could satisfy two fits, the same spectrum could be fit with illite instead of vermiculite with similar statistical results. Due to the difference in the XANES spectra between the two vermiculite standards [26], which theoretically should look the same since they have a similar chemical formula, we opted to use fits with illite instead of vermiculite until the discrepancies between vermiculite standards are resolved.

Principal component analysis of all experimental XANES spectra was performed in SIXpack in order to determine the spectra that are most dissimilar from one other, but together describe the entire XANES dataset, termed end-members. The K chemistries present in the end-members were determined using LCF (Figure 3), and these end-member spectra were fit to the multi-energy maps using a non-negative least squares fitting. The

number of chemical species that can be mapped using a least squares fitting of XANES spectra to multi-energy maps is n - 1 (where n is the number of mapped energies). For maps within the channel (Figure 1), five X-ray energies were mapped with a maximum of four chemical species that can be generated via least squares fitting. Due to the frequency of the presence of montmorillonite in the LCF of all spectra, and that illite was present in the end-members generally as a low abundance component of a mixture, montmorillonite was chosen for XRF map fitting over illite. Maps outside of the channel had additional energies based on features observed in XANES spectra from within the channel, allowing for 5 chemical species to be mapped in this region (Figure S2). The benefit of applying a non-linear least squares XANES fitting to multi-energy XRF images is that this process can provide the proportion of each chemical species identified in LCF to every pixel on the map without having to obtain a XANES spectrum at every pixel [31].

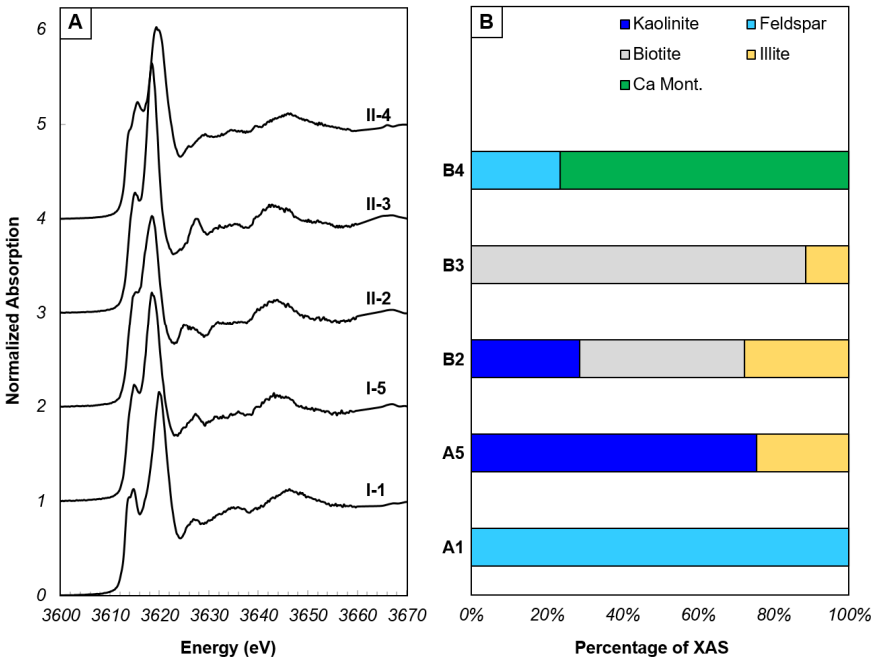

Figure 3. End-member potassium XANES spectra identified by PCA of XANES spectra from regions I and II. (**A**) End-member XANES spectra. (**B**) Proportions of minerals that comprise each end-member XANES spectrum, determined by LCF.

3. Results

Optical microscopy demonstrated that fungal hyphae grow towards the secondary C-rich nutrient port at the opposite end of the channel from the inoculation point (Figure 1A). K-associated with kaolinite, K-feldspar, and mica are considered primary minerals (Figure 1B,E) based on previous X-ray diffraction (XRD) data of the natural kaolinite powder embedded in the SSH [23]. Although kaolinite ($Al_2Si_2O_5(OH)_4$) does not contain K ions, the kaolinite XANES spectrum differs from micas (both biotite and muscovite) and K-feldspar, suggesting that K may incorporate into kaolinite mineral defects or may be sorbed to kaolinite (Figure S1) [30,32]. Therefore, kaolinite the in μ-XRF images represents K associated with kaolinite.

Secondary minerals identified via LCF of standard XANES spectra [26] to the experimental XANES include montmorillonite and illite (Figure 2C). At 3620 eV the X-ray beam will penetrate silicate minerals up to 10 μm, and the particle size for the natural kaolinite was 3–50 μm. Given that almost all LCF from within the SSH channel indicate the presence of a primary and secondary mineral at a given spot (Figure 2C) and considering an X-ray penetration depth of ~10 μm, most secondary minerals must be coatings < 10 μm

thick on the primary mineral surface. Additionally, the density of PDMS is lower than the density of silicate minerals, allowing X-rays to penetrate through the surface of the PDMS to minerals not exposed on the SSH surface. The abundance of kaolinite in all XRF images is likely contributions of minerals at depth in the PDMS. The distribution of montmorillonite differs depending on the location on the SSH. In the region of greater hyphal density (region I; Figure 1B–D), montmorillonite co-locates on most of the K-feldspar grains, surrounds and co-locates on some kaolinite grains, and co-locates on a handful of biotite grains. In comparison, where there was less hyphal density (region II; Figure 1E–G), montmorillonite is mostly found to co-locate with kaolinite and biotite, and less commonly with K-feldspar. To ensure that secondary mineral formation did not occur due to DRIE or mineral exposure to air, we collected XRF images and XANES spectra on a region outside of the SSH channel, where fungal growth did not occur, as a control. In the control region, we observed variable distributions of the primary minerals kaolinite, K-feldspar, and biotite (Figure S2A) similar to the distribution within the channel. Both XRF map fitting and LCF (Figure S2B–D) indicate minimal contributions of secondary minerals illite and a synthetic montmorillonite. Synthetic montmorillonite was used in LCF due to the similarity between previously published synthetic montmorillonite [26] and natural montmorillonite [28]; no synthetic montmorillonite was used in the SSH fabrication. These phases are spatially isolated in the region and do not co-locate with any primary mineral (Figure S2A,B).

The XANES spectra from the SSH can be generally described by the following features: (1) a single or double pre-edge feature occurring between 3613.7 and 3616.0 eV on the rising edge, (2) a white line position between 3618.5 and 3620.5 eV and (3) up to three post-edge features between 3625 and 3650 eV (Figures 2A,B, and S2C). The energy position (and shape) of the pre-edge feature and white line, and the presence of post-edge features varies across the SSH, owing to changing proportions of the mineralogy at spot locations within the imaged areas. Within the SSH channel, the most abundant mineral in the XANES spectra is kaolinite (since the kaolinite standard used in the LCF is the same natural kaolinite powder as that embedded in the SSH initially), typically comprising > 25% of most of the spectra. Other primary minerals, K-feldspar and biotite are less abundant, consistent with XRD results [23]. When present, feldspar comprises 23.5–100% of a spectrum, while biotite comprises 16.7–88.6% of a spectrum. Montmorillonite is present from 12.2 to 33.1%, and up to 76.4% in one spectrum. Illite is present in fewer spectra than montmorillonite but is present at a similar range of abundances from 11.4 to 76.5%. In comparison, XANES spectra from outside the channel were varying mixtures of kaolinite (9.5–77.2%) K-feldspar (38.2–100%) and biotite (41.4–100%). Contributions from montmorillonite and illite were minor, present in only one spectrum. It should be noted that the spectra which are fit by 100% K-feldspar have a higher R-factor than all other fit results (Table S1).

4. Discussion

4.1. Potassium XANES Spectroscopy in Environmental Samples

Potassium XANES spectroscopy has primarily been used to interrogate K coordination in micas [26,33–35] and silicate glasses [36,37], and the role of K in catalyst activity [38,39]. More recent studies have applied K XANES spectroscopy to environmental samples [30,40]. These studies have generated larger K XANES datasets from standard materials and minerals that are expected to be present in soil [30,32]. Of particular importance is the addition of clay minerals to these K XANES datasets. However, there are a few discrepancies in the spectroscopic features associated with certain clay minerals between the two datasets, likely due to the complex chemical composition of clays. Although K always remains in the same oxidation state (+1), K XANES spectra are rich in features. This is ideal for using K XANES spectroscopy for fingerprinting K chemistries within a sample. Char-

acteristics of K XANES spectra of minerals may include a number of the following features: (1) the presence of a low-energy pre-edge on a higher-intensity pre-edge feature, indicating 1s to 3d orbital splitting [41]; (2) pre-edge feature ~3 eV below the white line attributed to 1s to 4s orbital splitting [42,43]; (3) white line energy (1s to 4p) [41,43] position related to K coordination number, more specifically K-O bond distance [44]; (4) presence of a sharp post-edge feature approximately 8 eV above the white line position, possibly a result of photoelectron interaction with Fe atoms [26]; (5) splitting of the post-edge feature approximately 8 eV above the white line position into two lower-intensity features; and (6) the absence of post-edge features (with the exception of one broad feature approximately 27 eV above the white line present in essentially all spectra) that has been attributed to interlayer water or a decrease in structural ordering [30,32].

Experimental XANES spectra that are poorly fit and/or visibly deviate from available standards indicate that the standard dataset is not broad enough. However, in the case of SSH, appropriate standards of both primary and anticipated secondary K-bearing minerals were supplied (kaolinite, K-feldspar, biotite and muscovite, and montmorillonite, illite, and vermiculite, respectively), yet at least three spectra have features unknown from standards (I-1, II-1 and II-2; Figure 2A,B). Specifically, spectra I-1 and II-1 have a shift in the white line to higher by 2 eV, and spectrum II-2 has a post-edge feature closer in energy to the white line than all other spectra. A shift in the white line to higher energy is observed in K-feldspar XANES spectra [30,44] related to a change in K-O bond distance [40]. In the standard XANES spectra, the energy increases by 0.6 eV between micas and illite, and montmorillonite, and by 0.35 eV between montmorillonite and orthoclase (Figure S1), totaling at most 1 eV. In the case of I-1 and II-1 from the SSH, a white line shift of 2 eV to higher energy suggests a greater change to the K-O bond distance, perhaps related to altering the local K coordination environment due to ion exchange, the expected first phase of K-feldspar alteration [45].

Post-edge features are multiple scattering features of the ejected photoelectron interacting with surrounding atoms. Mica group minerals, illite, and vermiculite have the greatest number of defined post-edge features (Figure S2) with three features that generally overlap between these mineral groups at approximately 3628.0, 3634.5 and 3644.0 eV. Biotite and illite display a splitting of the first post-edge feature (3628.0 eV) with a lower-intensity feature at 3625.5 eV on the larger feature at 3628.0 eV. Both biotite and illite contain higher abundances of Mg and Fe compared to muscovite and phlogopite; therefore, it is possible that the increased abundance of other cations may distort the arrangement of the first shell K-O environment, leading to differences in the immediate post-edge. In spectrum II-2, the feature at 3625.5 eV is more intense than the feature at 3628.0 eV and is poorly fit by LCF, indicating that there are chemical compositions not captured by the available XANES spectroscopy databases, and/or the SSH experiments can capture intermediate stages of alteration between primary mineral and secondary mineral precipitates. However, mica anisotropy can affect the intensity and position of the first post-edge feature in phlogopite and zinnwaldite [33–35], yet this has not been replicated in biotite to our knowledge (the dominant mica in the SSH).

4.2. Impact of Fungal Exudates on Mineral Weathering

Due to the presence of montmorillonite and illite detected by XANES spectroscopy and XRF imaging, weathering of the primary SSH minerals must have occurred. In the controlled SSH environment: (1) temperature remained constant; (2) the SSH are microfluidic devices and the volume of solution is not representative of soil pore water; (3) grain size is between 3 and 50 μm and the amount of a grain exposed by DRIE cannot be quantified; (4) there are no oxide coatings on the mineral grains. Each of these factors can impact the rate of K-feldspar and mica weathering [46,47]. We therefore focus our discussion on biological activity on K mineral weathering.

Rhizosphere biological activity can impact the soil structure and chemical composition both directly and indirectly. Direct mechanisms include the mechanical breakdown

of soil minerals by plant roots and microbes moving through cracks and existing weak points in mineral grains, fungal osmotic pressure and expansion and contraction during wetting–drying cycles. Indirect activity typically relates to chemical changes such as pH or cation availability, which is a result of the production of plant and microbe respiration and exudates [48]. Low molecular weight organic acids (LMWOAs) are produced by most soil microbes and by plant roots. The abundance of plant and/or microbially exuded LMWOAs in bulk soil tend to be lower than what is required for mineral dissolution [49]. However, hotspots of organic acids are present in the rhizosphere and, where present, must be concentrated within microns of a mineral surface to promote mineral weathering [50]. In a reduced-complexity C-limited SSH, where the only source of nutrients was in K-rich minerals, saprotrophic fungi were observed to spatially focus the exudation of various LMWOAs depending on the proximity to a C-source [24]. In addition, the production and spatial differentiation of the organic acids was observed after 7 days of fungal growth in the SSH over approximately 2 cm of the SSH surface. The abundance, spatial differentiation, and spatial distribution of LMWOAs increased over 30 days (covering up to 5 cm of the SSH surface) [24]. Other studies have shown fungal production of LMWOAs occurs within hours, depending on the concentration and form of C source [51], and within 2 days in the presence of minerals [52].

It is known that organic acids, particularly oxalic acid, increases feldspar dissolution rates in laboratory studies when compared to inorganic acids [53], as well as other silicate minerals [52,54]. Citric, tartaric, succinic, pyruvic, and acetic acids have also been observed to play a role in the dissolution of Ca-feldspar, K-feldspar, micas, and clays [55–58] at rates 10 times greater than inorganic acids alone. The expectation of organic acid weathering of K-feldspar is that kaolinite, muscovite, vermiculite, illite, or smectite clays can form as K-rich secondary mineral products [47,59]. Similarly, biotite weathering products include vermiculite and smectite, both of which can form secondary kaolinite. Over longer timescales, kaolinite will weather to smectitie, illite, and/or chlorite [47]. An *Aspergillus* fungal strain was observed to produce more tartaric acid than any other LMWOA in vertisol (clay dominant soil) compared to alfi- and andisols [60], and bacterial tartrate production, along with malate, has shown to be effective in rare earth element mobilization from granite [61]. Other KSM have been observed to produce more tartaric acid than other LMWOAs, although the type and abundance of LMWOA production by fungi appears to be strain and/or soil/mineral specific [62]. Previously, we have observed the production of citric, tartaric, malic, fumaric, oxalic, and succinic acids by *Fusarium sp. DS 682* in the presence of natural kaolinite. Citric, tartaric, malic, and fumaric acids were the most abundant and varied spatially within the SSH in response to C limitation. The co-localization of tartaric acid with glycogen at greater distances from the only C source was suggested to be the result in a change in fungal metabolic pathway during C limitation [24].

Given the spatial differences in secondary clay formation between the two regions of the SSH, and spatial differentiation of organic acids, it is possible that the organic acids are playing distinct roles in the weathering process. Montmorillonite is more frequently co-located on feldspar in region I, and a higher abundance of citric, malic, and fumaric acids have been observed in the central region of the SSH [24]. Citric acid production relies on the availability of Mn, Fe, and Zn [63]. The main source of any of these metals in the SSH could be either PDA or Fe from biotite, or trace metal substitutions into K-feldspar or biotite. Previous observations noted both citric and malic acid were produced in greater abundance by mycorrhizal fungi when in the presence of biotite versus feldspar [16]. Yet, a number of studies report that citric is as effective as oxalic acid in feldspar weathering, which are both more effective than other organic acids [55,56]. In our case, hyphae closer to the C source (region I) may have increased citrate production due to the greater availability of organic C (in the PDA plug at the inoculation point) for the tricarboxylic acid (TCA) cycle, where both Fe and Mn are available in PDA and as trace components of minerals within the SSH. Along with fumaric and malic acid, produced as part of the TCA cycle, citric acid is effective at feldspar weathering in these central regions of the SSH, in

proximity to the C source. When limited by C, fungi at greater distances from the C-source switch to tartaric acid production. Since tartaric acid is less effective at weathering feldspar, a decrease in the co-location of feldspar and montmorillonite is observed with a coincident increase in montmorillonite precipitate on biotite. In both regions, montmorillonite on kaolinite appears equivalent, suggesting that the impact of the available LMWOAs on kaolinite is similar over 30 days. These data indicate that organic C availability ultimately controls the effectiveness of *Fusarium sp. DS 682* in the bio-weathering of K from feldspars.

4.3. Implications for the Holistic Rhizosphere

Fusarium sp. DS 682 is a saprotrophic fungus that can grow on any available organic C source without the need for plant C exchange. Previously we have demonstrated *Fusarium sp. DS 682* can: (1) bridge spatially disconnected C hotspots only when soil minerals are present, (2) upregulate transporter proteins for transmembrane transport of LMWOAs [23], and (3) spatially differentiate LMWOA exudation depending on distance from a C hotspot [24]. Here, we have demonstrated the impact of *Fusarium sp. DS 682* LMWOA exudation on K-rich minerals after 30 days of hyphal growth. Specifically, in the formation of 10s of μm sized secondary clay mineral coatings on primary K mineral grains. This approach indicates that *Fusarium sp. DS 682* enhances the movement of K between rhizosphere K pools, from the non-bioavailable structurally bound K pool to the readily available pool in hydrated secondary mineral interlayers during C limitation. Increasing the abundance of K in hydrated secondary clay mineral interlayers increases the likelihood of exchange of interlayer K with solution K that can be used by plants. Additionally, K sorbed to fungal exudates provides an additional bioavailable K pool.

There are a number of studies of the role of mycorrhizal (including arbuscular and ectomycorrhizal) fungi in plant potassium nutrition [16,64–66]. However, mycorrhizal metabolic processes rely on C exchange from plants, rather than from other forms of soil C, and as a result a number of these fungal metabolic processes may go untriggered when C is not supplied by plants [67]. In contrast, saprotrophs do not require a nutrient exchange in return from plants and there are some of studies of the impact of the presence of saprotrophic fungal species in soil on plant biomass K [10,68]. Similarly, there are several studies investigating the role of K solubilizing bacteria and associations to plant potassium [15,69,70]. Many of these studies focus on single species relationships, with fewer introducing more complex microbiomes [71]. Since the plant microbiome is a complex holobiont, combined with the heterogeneity of soil geochemistry, it is likely that saprotroph organic acid exudation and induced mineral weathering could affect other microbes, such as the proliferation of other microbial metabolisms by release of various elements from soil minerals. Increasing biological complexity in the SSH will facilitate future studies of the relationship between *Fusarium sp. DS 682*, plant roots and other microbes.

The formation of clays can impact local soil organic matter (SOM) recalcitrance. Clay minerals provide stabilization for SOM through increasing the abundance of microaggregates, increasing the available reactive surface area due to small clay particle sizes, and clay cation exchange capacity improves surface sorption [72,73]. Smectite clays can enhance adsorbed C compared to illite and kaolinite. Moreover, while kaolinite tends to be stable over long timescales, montmorillonite has a high effective surface area and cation exchange capacity that makes it more effective at sorption [73]. Further, montmorillonite is more effective at sorbing low molecular weight organic compounds compared to Fe oxyhydroxides [74]. Given the growing number of environmental K investigations using XANES spectroscopy, K XANES spectroscopy could be useful for understanding clay-OM interactions for future investigations on soil C sequestration by KSM- and K-rich minerals.

5. Conclusions

Synthetic soil habitats that are compatible with synchrotron XRF imaging beamlines provide an ideal platform to study biogeochemical soil processes on environmentally relevant spatial and temporal scales. The saprotroph *Fusarium sp. DS 682* sources potassium from minerals by regulating the type of organic acid it produces depending on the proximity to a C hotspot. The result of organic acid interaction with primary minerals is the formation of secondary clays, where K is exchangeable within clay interlayers more readily than it is when structurally bound within primary minerals feldspar and biotite. The size of clay mineral coatings is proportional to the grain size of primary minerals (10s of μm). A change in the distribution of secondary clays on primary minerals is observed depending on distance to the principal C source, consistent with changing fungal metabolic processes. Potassium XANES spectroscopy can identify intermediate stages of primary mineral alteration prior to secondary mineral precipitation and thus is a useful probe into the mechanisms controlling K bioavailability in the environment.

Supplementary Materials: The following supporting information can be downloaded at: https://mdpi.com/xxx/s1, Table S1: Linear combination fitting results; Figure S1: XANES spectra of standard minerals; Figure S2: XRF maps and XANES spectra from outside of the microfluidic channel.

Author Contributions: Conceptualization, A.B. and C.R.A.; methodology, A.B. and J.A.R.; formal analysis, J.A.R.; investigation, A.B. and J.A.R.; data curation, J.A.R.; writing—original draft preparation, J.A.R.; writing—review and editing, all authors; visualization, J.A.R.; funding acquisition, A.B. and J.A.R. All authors have read and agreed to the published version of the manuscript.

Funding: This research was performed on a project award (10.46936/intm.proj.2021.60094/60001433) from the Environmental Molecular Sciences Laboratory, a DOE Office of Science User Facility sponsored by the Biological and Environmental Research program under Contract No. DE-AC05-76RL01830.

Data Availability Statement: Data supporting this research can be located at https://purl.stanford.edu/hm844rq5533, made available on 23 March 2023.

Acknowledgments: Use of the Stanford Synchrotron Radiation Lightsource (SSRL), SLAC National Accelerator Laboratory, is supported by the DOE, Office of Science, Office of Basic Energy Sciences under contract DE-AC02-76SF00515. The SSRL Structural Molecular Biology Program is supported by the DOE-BER, and by the National Institutes of Health (NIH), National Institute of General Medical Sciences (NIGMS; P30GM133894). The contents of this publication are solely the responsibility of the authors and do not necessarily represent the official views of the NIGMS or the NIH. J.R is supported by supplemental funding from DOE-BER to assist and expand biological and environmental relevant research and users at SSRL. We thank M. Siebecker for providing raw XANES spectra of standard materials.

Conflicts of Interest: The authors declare no conflict of interest.

References

1. Jones, K.; Nti, F. *Impacts and Repercussions of Price Increases on the Global Fertilizer Market* ; 2022;
2. Vermeulen, S.J.; Campbell, B.M.; Ingram, J.S.I. Climate Change and Food Systems. *Annu Rev Environ Resour* **2012**, *37*, 195–222, doi:10.1146/annurev-environ-020411-130608.
3. Britzke, D.; da Silva, L.S.; Moterle, D.F.; dos Santos Rheinheimer, D.; Bortoluzzi, E.C. A Study of Potassium Dynamics and Mineralogy in Soils from Subtropical Brazilian Lowlands. *J Soils Sediments* **2012**, *12*, 185–197, doi:10.1007/s11368-011-0431-7.
4. Sparks, D.L. Potassium Dynamics in Soils. In *Advances in Soil Science*; 1987; pp. 1–63.
5. Mikkelsen, R.L. Managing Potassium for Organic Crop Production. *Horttechnology* **2007**, *17*, 455–460, doi:10.21273/horttech.17.4.455.

6. Römheld, V.; Kirkby, E.A. Research on Potassium in Agriculture: Needs and Prospects. *Plant Soil* **2010**, *335*, 155–180, doi:10.1007/s11104-010-0520-1.
7. Sattar, A.; Naveed, M.; Ali, M.; Zahir, Z.A.; Nadeem, S.M.; Yaseen, M.; Meena, V.S.; Farooq, M.; Singh, R.; Rahman, M.; et al. Perspectives of Potassium Solubilizing Microbes in Sustainable Food Production System: A Review. *Applied Soil Ecology* **2019**, *133*, 146–159, doi:10.1016/j.apsoil.2018.09.012.
8. Lasaga, A.C. Chemical Kinetics of Water-Rock Interactions. *J Geophys Res Solid Earth* **1984**, *89*, 4009–4025, doi:10.1029/JB089iB06p04009.
9. Manning, D.A.C. Innovation in Resourcing Geological Materials as Crop Nutrients. *Natural Resources Research* **2018**, *27*, 217–227, doi:10.1007/s11053-017-9347-2.
10. Li, X.; Yin, Y.; Fan, S.; Xu, X.; Amombo, E.; Xie, Y.; Fu, J. *Aspergillus Aculeatus* Enhances Potassium Uptake and Photosynthetic Characteristics in Perennial Ryegrass by Increasing Potassium Availability. *J Appl Microbiol* **2022**, *132*, 483–494, doi:10.1111/jam.15186.
11. Lian, B.; Wang, B.; Pan, M.; Liu, C.; Teng, H.H. Microbial Release of Potassium from K-Bearing Minerals by Thermophilic Fungus Aspergillus Fumigatus. *Geochim Cosmochim Acta* **2008**, *72*, 87–98, doi:10.1016/j.gca.2007.10.005.
12. Paris, F.; Bernard, B.; Lapeyrie, F. In Vitro Weathering of Phlogopite by Ectomycorrhizal Fungi II. Effect of K + and Mg 2+ Deficiency and N Sources on Accumulation of Oxalate and H +. *Plant Soil* **1996**, *179*.
13. Paris, F.; Bonnaud, P.; Ranger, J.; Lapeyrie, F. In Vitro Weathering of Phlogopite by Ectomycorrhizal Fungi—I. Effect of K+ and Mg2+ Deficiency on Phyllosilicate Evolution. *Plant Soil* **1995**, *177*, 191–201, doi:10.1007/BF00010125.
14. Pinzari, F.; Cuadros, J.; Jungblut, A.D.; Najorka, J.; Humphreys-Williams, E. Fungal Strategies of Potassium Extraction from Silicates of Different Resistance as Manifested in Differential Weathering and Gene Expression. *Geochim Cosmochim Acta* **2022**, *316*, 168–200, doi:10.1016/j.gca.2021.10.010.
15. Sheng, X.F. Growth Promotion and Increased Potassium Uptake of Cotton and Rape by a Potassium Releasing Strain of Bacillus Edaphicus. *Soil Biol Biochem* **2005**, *37*, 1918–1922, doi:10.1016/j.soilbio.2005.02.026.
16. Wallander, H.; Wickman, T. Biotite and Microcline as Potassium Sources in Ectomycorrhizal and Non-Mycorrhizal Pinus Sylvestris Seedlings. *Mycorrhiza* **1999**, *9*, 25–32, doi:10.1007/s005720050259.
17. Hu, X.; Chen, J.; Guo, J. Two Phosphate- and Potassium-Solubilizing Bacteria Isolated from Tianmu Mountain, Zhejiang, China. *World J Microbiol Biotechnol* **2006**, *22*, 983–990, doi:10.1007/s11274-006-9144-2.
18. Finlay, R.D.; Mahmood, S.; Rosenstock, N.; Bolou-Bi, E.B.; Köhler, S.J.; Fahad, Z.; Rosling, A.; Wallander, H.; Belyazid, S.; Bishop, K.; et al. Reviews and Syntheses: Biological Weathering and Its Consequences at Different Spatial Levels - From Nanoscale to Global Scale. *Biogeosciences* **2020**, *17*, 1507–1533, doi:10.5194/bg-17-1507-2020.
19. Shirale, A.O.; Meena, B.P.; Gurav, P.P.; Srivastava, S.; Biswas, A.K.; Thakur, J.K.; Somasundaram, J.; Patra, A.K.; Rao, A.S. Prospects and Challenges in Utilization of Indigenous Rocks and Minerals as Source of Potassium in Farming. *J Plant Nutr* **2019**, *42*, 2682–2701, doi:10.1080/01904167.2019.1659353.
20. Wild, B.; Daval, D.; Beaulieu, E.; Pierret, M.-C.; Viville, D.; Imfeld, G. In-Situ Dissolution Rates of Silicate Minerals and Associated Bacterial Communities in the Critical Zone (Strengbach Catchment, France). *Geochim Cosmochim Acta* **2019**, *249*, 95–120, doi:10.1016/j.gca.2019.01.003.
21. Song, M.; Pedruzzi, I.; Peng, Y.; Li, P.; Liu, J.; Yu, J. K-Extraction from Muscovite by the Isolated Fungi. *Geomicrobiol J* **2015**, *32*, 771–779, doi:10.1080/01490451.2014.985409.

22. Lybrand, R.A.; Austin, J.C.; Fedenko, J.; Gallery, R.E.; Rooney, E.; Schroeder, P.A.; Zaharescu, D.G.; Qafoku, O. A Coupled Microscopy Approach to Assess the Nano-Landscape of Weathering. *Sci Rep* **2019**, *9*, 5377, doi:10.1038/s41598-019-41357-0.
23. Bhattacharjee, A.; Qafoku, O.; Richardson, J.A.; Anderson, L.N.; Schwarz, K.; Bramer, L.M.; Lomas, G.X.; Orton, D.J.; Zhu, Z.; Engelhard, M.H.; et al. A Mineral-Doped Micromodel Platform Demonstrates Fungal Bridging of Carbon Hot Spots and Hyphal Transport of Mineral-Derived Nutrients. *mSystems* **2022**, *7*, doi:10.1128/msystems.00913-22.
24. Bhattacharjee, A.; Velickovic, D.; Richardson, J.A.; Couvillion, S.P.; Vandergrift, G.W.; Qafoku, O.; Taylor, M.J.; Jansson, J.K.; Hofmockel, K.S.; Anderton, C.R. Fungal Organic Acid Uptake of Mineral Derived K Is Dependent on Distance from Carbon Hotspot. *biorxiv* **2023**, doi:doi.org/10.1101/2023.03.17.533228.
25. Bhattacharjee, A.; Anderson, L.N.; Alfaro, T.; Porras-Alfaro, A.; Jumpponen, A.; Hofmockel, K.S.; Jansson, J.K.; Anderton, C.R.; Nelson, W.C. Draft Genome Sequence of Fusarium Sp. Strain DS 682, a Novel Fungal Isolate from the Grass Rhizosphere . *Microbiol Resour Announc* **2021**, *10*, doi:10.1128/mra.00884-20.
26. Cibin, G.; Mottana, A.; Marcelli, A.; Brigatti, M.F. Potassium Coordination in Trioctahedral Micas Investigated by K-Edge XANES Spectroscopy. *Mineral Petrol* **2005**, *85*, 67–87, doi:10.1007/s00710-005-0099-z.
27. Webb, S.M. SIXPack a Graphical User Interface for XAS Analysis Using IFEFFIT. *Phys Scr* **2005**, *2005*, 1011, doi:10.1238/Physica.Topical.115a01011.
28. Ravel, B.; Newville, M. ATHENA, ARTEMIS, HEPHAESTUS: Data Analysis for X-Ray Absorption Spectroscopy Using IFEFFIT. In Proceedings of the Journal of Synchrotron Radiation; July 2005; Vol. 12, pp. 537–541.
29. Webb, S.M. SMAK: Sam's Microprobe Analysis Kit, V 0.46; Stanford Synchrotron Radiation Laboratory: Stanford, CA 2006.
30. Schmidt, E.J.; Zanoni, G.; Bumguardner, A.; Šegvić, B.; Lewis, K.; Abdala, D.; Siebecker, M.G. Soil Chemical Extractions Can Alter Potassium Coordination in Agricultural Soils: A Combined Wet Chemical and X-Ray Absorption Spectroscopic Approach. *Geoderma* **2022**, *422*, doi:10.1016/j.geoderma.2022.115914.
31. Marcus, M.A. X-Ray Photon-in/Photon-out Methods for Chemical Imaging. *TrAC - Trends in Analytical Chemistry* **2010**, *29*, 508–517, doi:10.1016/j.trac.2010.02.013.
32. Li, W.; Liu, X.M.; Hu, Y. Potassium and Calcium K-Edge XANES in Chemical Compounds and Minerals: Implications for Geological Phase Identification. *Geostand Geoanal Res* **2020**, *44*, 805–819, doi:10.1111/ggr.12351.
33. Brigatti, M.F.; Malferrari, D.; Poppi, M.; Mottana, A.; Cibin, G.; Marcelli, A.; Cinque, G. Interlayer Potassium and Its Neighboring Atoms in Micas: Crystal-Chemical Modeling and XANES Spectroscopy. *American Mineralogist* **2008**, *93*, 821–830, doi:10.2138/am.2008.2644.
34. Xu, W.; Chen, D.; Chu, W.; Wu, Z.; Marcelli, A.; Mottana, A.; Soldatov, A.; Brigatti, M.F. Quantitative Local Structure Determination in Mica Crystals: Ab Initio Simulations of Polarization XANES at the Potassium K-Edge. *J Synchrotron Radiat* **2011**, *18*, 418–426, doi:10.1107/S0909049511002949.
35. Cibin, G.; Mottana, A.; Marcelli, A.; Brigatti, M.F. Angular Dependence of Potassium K-Edge XANES Spectra of Trioctahedral Micas: Significance for the Determination of the Local Structure and Electronic Behavior of the Interlayer Site. *American Mineralogist* **2006**, *91*, 1150–1162, doi:10.2138/am.2006.2041.
36. Ragoen, C.; Cormier, L.; Bidegaray, A.-I.; Vives, S.; Henneman, F.; Trcera, N.; Godet, S. A XANES Investigation of the Network-Modifier Cations Environment before and after the Na + /K + Ion-Exchange in Silicate Glasses. *J Non Cryst Solids* **2018**, *479*, 97–104, doi:10.1016/j.jnoncrysol.2017.10.021.

37. Jackson, W.E.; Brown, G.E.; Ponader, C.W. X-Ray Absorption Study of the Potassium Coordination Environment in Glasses from the NaAlSi3O8-KAlSi3O8 Binary. *J Non Cryst Solids* **1987**, *93*, 311–322, doi:10.1016/S0022-3093(87)80177-1.
38. Davies, C.J.; Mayer, A.; Gabb, J.; Walls, J.M.; Degirmenci, V.; Thompson, P.B.J.; Cibin, G.; Golunski, S.; Kondrat, S.A. Operando Potassium K-Edge X-Ray Absorption Spectroscopy: Investigating Potassium Catalysts during Soot Oxidation. *Physical Chemistry Chemical Physics* **2020**, *22*, 18976–18988, doi:10.1039/d0cp01227k.
39. Jacobs, G.; Pendyala, V.R.R.; Martinelli, M.; Shafer, W.D.; Gnanamani, M.K.; Khalid, S.; MacLennan, A.; Hu, Y.; Davis, B.H. Fischer–Tropsch Synthesis: XANES Spectra of Potassium in Promoted Precipitated Iron Catalysts as a Function of Time On-Stream. *Catal Letters* **2017**, *147*, 1861–1870, doi:10.1007/s10562-017-2090-9.
40. Li, W.; Liu, X.M.; Hu, Y.; Teng, F.Z.; Hu, Y.F.; Chadwick, O.A. Potassium Isotopic Fractionation in a Humid and an Arid Soil–Plant System in Hawai'i. *Geoderma* **2021**, *400*, doi:10.1016/j.geoderma.2021.115219.
41. Xu, F.; Huang, Z.; Hu, P.; Chen, Y.; Zheng, L.; Gao, J.; Tang, X. The Promotion Effect of Isolated Potassium Atoms with Hybridized Orbitals in Catalytic Oxidation. *Chemical Communications* **2015**, *51*, 9888–9891, doi:10.1039/C5CC02476E.
42. Dutta, C.M.; Huang, H.W. K-Edge Absorption Spectra of Ionic Potassium and Its Z+1 Analogy. *Phys Rev Lett* **1980**, *44*, 643–646, doi:10.1103/PhysRevLett.44.643.
43. Sugiura, C.; Muramatsu, S. K-Edge X-Ray Absorption Spectra from Potassium Compounds. *physica status solidi (b)* **1985**, *132*, K111–K115, doi:10.1002/pssb.2221320249.
44. Spiro, C.L.; Wong, J.; Lytle, F.W.; Greegor, R.B.; Maylotte, D.H.; Lamson, S.H. Forms of Potassium in Coal and Its Combustion Products. *Fuel* **1986**, *65*, 327–336, doi:10.1016/0016-2361(86)90291-7.
45. Skorina, T.; Allanore, A. Aqueous Alteration of Potassium-Bearing Aluminosilicate Minerals: From Mechanism to Processing. *Green Chemistry* **2015**, *17*, 2123–2136, doi:10.1039/c4gc02084g.
46. Yuan, G.; Cao, Y.; Schulz, H.-M.; Hao, F.; Gluyas, J.; Liu, K.; Yang, T.; Wang, Y.; Xi, K.; Li, F. A Review of Feldspar Alteration and Its Geological Significance in Sedimentary Basins: From Shallow Aquifers to Deep Hydrocarbon Reservoirs. *Earth Sci Rev* **2019**, *191*, 114–140, doi:10.1016/j.earscirev.2019.02.004.
47. Wilson, M.J. Weathering of the Primary Rock-Forming Minerals: Processes, Products and Rates. *Clay Miner* **2004**, *39*, 233–266, doi:10.1180/0009855043930133.
48. Hoffland, E.; Kuyper, T.W.; Wallander, H.; Plassard, C.; Gorbushina, A.A.; Haselwandter, K.; Holmström, S.; Landeweert, R.; Lundström, U.S.; Rosling, A.; et al. The Role of Fungi in Weathering Available online: https://esajournals.onlinelibrary.wiley.com/doi/epdf/10.1890/1540-9295%282004%29002%5B0258%3ATROFIW%5D2.0.CO%3B2?saml_referrer (accessed on 26 May 2022).
49. Drever, J.I.; Vance, G.F. Role of Soil Organic Acids in Mineral Weathering Processes. In *Organic Acids in Geological Processes*; Springer Berlin Heidelberg: Berlin, Heidelberg, 1994; pp. 138–161.
50. Smits, M.M. Scale Matters? Exploring the Effect of Scale on Fungal–Mineral Interactions. *Fungal Biol Rev* **2009**, *23*, 132–137, doi:10.1016/j.fbr.2009.11.002.
51. Dörsam, S.; Fesseler, J.; Gorte, O.; Hahn, T.; Zibek, S.; Syldatk, C.; Ochsenreither, K. Sustainable Carbon Sources for Microbial Organic Acid Production with Filamentous Fungi. *Biotechnol Biofuels* **2017**, *10*, doi:10.1186/s13068-017-0930-x.

52. Li, Z. bo; Lu, X.; Teng, H.H.; Chen, Y.; Zhao, L.; Ji, J.; Chen, J.; Liu, L. Specificity of Low Molecular Weight Organic Acids on the Release of Elements from Lizardite during Fungal Weathering. *Geochim Cosmochim Acta* **2019**, *256*, 20–34, doi:10.1016/j.gca.2018.09.029.
53. Stillings, L.L.; Drever, J.I.; Brantley, S.L.; Sun, Y.; Oxburgh, R. Rates of Feldspar Dissolution at PH 3-7 with 0-8 m M Oxalic Acid. *Chem Geol* **1996**, *132*, 79–89, doi:10.1016/S0009-2541(96)00043-5.
54. Schmalenberger, A.; Duran, A.L.; Bray, A.W.; Bridge, J.; Bonneville, S.; Benning, L.G.; Romero-Gonzalez, M.E.; Leake, J.R.; Banwart, S.A. Oxalate Secretion by Ectomycorrhizal Paxillus Involutus Is Mineral-Specific and Controls Calcium Weathering from Minerals. *Sci Rep* **2015**, *5*, doi:10.1038/srep12187.
55. Huang, W.H.; Keller, W.D. Organic Acids as Agents of Chemical Weathering of Silicate Minerals. *Nature Physical Science* **1972**, *239*, 149–151, doi:10.1038/physci239149a0.
56. Manley, E.P.; Evans, L.J. Dissolution of Feldspars by Low-Molecular-Weight Aliphatic and Aromatic Acids. *Soil Sci* **1986**, *141*, 106–112, doi:10.1097/00010694-198602000-00002.
57. Wang, X.; Li, Q.; Hu, H.; Zhang, T.; Zhou, Y. Dissolution of Kaolinite Induced by Citric, Oxalic, and Malic Acids. *J Colloid Interface Sci* **2005**, *290*, 481–488, doi:10.1016/j.jcis.2005.04.066.
58. Welch, S.A.; Ullman, W.J. The Effect of Organic Acids on Plagioclase Dissolution Rates and Stoichiometry. *Geochim Cosmochim Acta* **1993**, *57*, 2725–2736, doi:10.1016/0016-7037(93)90386-B.
59. Eggleton, R.A.; Buseck, P.R. High Resolution Electron Microscopy of Feldspar Weathering. *Clays Clay Miner* **1980**, *28*, 173–178, doi:10.1346/CCMN.1980.0280302.
60. Zúñiga-Silgado, D.; Rivera-Leyva, J.C.; Coleman, J.J.; Sánchez-Reyez, A.; Valencia-Díaz, S.; Serrano, M.; De-Bashan, L.E.; Folch-Mallol, J.L. Soil Type Affects Organic Acid Production and Phosphorus Solubilization Efficiency Mediated by Several Native Fungal Strains from Mexico. *Microorganisms* **2020**, *8*, 1–17, doi:10.3390/microorganisms8091337.
61. He, Y.; Ma, L.; Li, X.; Wang, H.; Liang, X.; Zhu, J.; He, H. Mobilization and Fractionation of Rare Earth Elements during Experimental Bio-Weathering of Granites. *Geochim Cosmochim Acta* **2023**, doi:10.1016/j.gca.2022.12.027.
62. Islam, M.K.; Sano, A.; Majumder, M.S.I.; Sakagami, J.I.; Gima, S.; Hossain, M.A. Evaluation of Organic Acid Production Potential of Phosphate Solubilizing Fungi Isolated from Soils in Okinawa, Japan. *Appl Ecol Environ Res* **2019**, *17*, 15191–15201, doi:10.15666/aeer/1706_1519115201.
63. Gadd, G.M. Fungal Production of Citric and Oxalic Acid: Importance in Metal Speciation, Physiology and Biogeochemical Processes. *Adv Microb Physiol* **1999**, *41*, 47–92, doi:10.1016/s0065-2911(08)60165-4.
64. Van Schöll, L.; Smits, M.M.; Hoffland, E. Ectomycorrhizal Weathering of the Soil Minerals Muscovite and Hornblende. *New Phytologist* **2006**, *171*, 805–814, doi:10.1111/j.1469-8137.2006.01790.x.
65. Perner, H.; Schwarz, D.; Bruns, C.; Mäder, P.; George, E. Effect of Arbuscular Mycorrhizal Colonization and Two Levels of Compost Supply on Nutrient Uptake and Flowering of Pelargonium Plants. *Mycorrhiza* **2007**, *17*, 469–474, doi:10.1007/s00572-007-0116-7.
66. Garcia, K.; Zimmermann, S.D. The Role of Mycorrhizal Associations in Plant Potassium Nutrition. *Front Plant Sci* **2014**, *5*, doi:10.3389/fpls.2014.00337.
67. Fellbaum, C.R.; Gachomo, E.W.; Beesetty, Y.; Choudhari, S.; Strahan, G.D.; Pfeffer, P.E.; Kiers, E.T.; Bücking, H. Carbon Availability Triggers Fungal Nitrogen Uptake and Transport in Arbuscular Mycorrhizal Symbiosis. *Proceedings of the National Academy of Sciences* **2012**, *109*, 2666–2671, doi:10.1073/pnas.1118650109.

68. Peng, L.; Shan, X.; Yang, Y.; Wang, Y.; Druzhinina, I.S.; Pan, X.; Jin, W.; He, X.; Wang, X.; Zhang, X.; et al. Facultative Symbiosis with a Saprotrophic Soil Fungus Promotes Potassium Uptake in American Sweetgum Trees. *Plant Cell Environ* **2021**, *44*, 2793–2809, doi:10.1111/pce.14053.
69. Sheng, X.F.; He, L.Y. Solubilization of Potassium-Bearing Minerals by a Wild-Type Strain of Bacillus Edaphicus and Its Mutants and Increased Potassium Uptake by Wheat. *Can J Microbiol* **2006**, *52*, 66–72, doi:10.1139/w05-117.
70. Zhang, C.; Kong, F. Isolation and Identification of Potassium-Solubilizing Bacteria from Tobacco Rhizospheric Soil and Their Effect on Tobacco Plants. *Applied Soil Ecology* **2014**, *82*, 18–25, doi:10.1016/j.apsoil.2014.05.002.
71. Basak, B.B.; Biswas, D.R. Co-Inoculation of Potassium Solubilizing and Nitrogen Fixing Bacteria on Solubilization of Waste Mica and Their Effect on Growth Promotion and Nutrient Acquisition by a Forage Crop. *Biol Fertil Soils* **2010**, *46*, 641–648, doi:10.1007/s00374-010-0456-x.
72. Angst, G.; Mueller, K.E.; Nierop, K.G.J.; Simpson, M.J. Plant- or Microbial-Derived? A Review on the Molecular Composition of Stabilized Soil Organic Matter. *Soil Biol Biochem* **2021**, *156*, doi:10.1016/j.soilbio.2021.108189.
73. Churchman, G.J.; Singh, M.; Schapel, A.; Sarkar, B.; Bolan, N. Clay Minerals As the Key To the Sequestration of Carbon in Soils. *Clays Clay Miner* **2020**, *68*, 135–143, doi:10.1007/s42860-020-00071-z.
74. Han, L.; Yang, Y.; Sun, K.; Zhang, B.; Chen, Y.; Fang, L.; Xing, B. Different Mechanisms Driving the Preferential Adsorption of Dissolved Organic Matter by Goethite and Montmorillonite. *Chem Geol* **2021**, *585*, doi:10.1016/j.chemgeo.2021.120560.